Ultrafast Science
A SCIENCE PARTNER JOURNAL

RESEARCH ARTICLE

Femtosecond-Laser-Induced All-Silicon Dielectric Metasurfaces Assisted by Wet Chemical Etching

Ioanna Sakellari[1*], Sotiris Droulias[2], Andreas Lemonis[3], and Emmanuel I. Stratakis[1*]

[1]Institute of Electronic Structure and Laser, Foundation for Research and Technology Hellas, Heraklion, Crete, 71110, Greece. [2]University of Piraeus, Piraeus, 18534, Greece. [3]Biomimetic, Science and Technology Park of Crete, Heraklion, Crete, 70013, Greece.

*Address correspondence to: isakel@iesl.forth.gr (E.I.S.); stratak@iesl.forth.gr (I.S.)

Citation: Sakellari I, Droulias S, Lemonis A, Stratakis EI. Femtosecond-Laser-Induced All-Silicon Dielectric Metasurfaces Assisted by Wet Chemical Etching. *Ultrafast Sci.* 2023;3:Article 0019. https://doi.org/10.34133/ultrafastscience.0019

Submitted 20 November 2022
Accepted 20 January 2023
Published 14 March 2023

All-dielectric metasurfaces offer low material loss and strong field localization and are, therefore, well suited for ultrathin and compact optical devices for electomagnetic wave manipulation at the nanoscale. All-silicon dielectric metasurfaces, in particular, may additionally offer the desired compatibility with complementary metal-oxide semiconductor technology and, hence, are ideal candidates for large-scale monolithic integration on a photonic chip. However, in conventional silicon microfabrication approaches, the combination of mask photolithography with reactive ion etching usually involves expensive masks and multiple preprocessing stages leading to increased cost and fabrication times. In this work, a single-step lithographical approach is proposed for the realization of all-silicon dielectric resonant metasurfaces that involves femtosecond laser processing of silicon below ablation threshold in combination with subsequent wet chemical etching. The method exploits the different etching rate between laser-modified and untreated regions, enabling large-area fabrication of patterned silicon surfaces in a facile and cost-efficient manufacturing approach. It is presented how two-dimensional silicon micro/nanostructures with controllable features, such as nanocones, can be effectively generated and, as a proof of concept, an all-silicon dielectric metasurface device supporting antiferromagnetic order is experimentally demonstrated.

Introduction

Dielectric metasurfaces composed of high refractive index dielectric scatterers arranged into a 2-dimensional (2D) periodic array are capable of achieving simultaneous phase and polarization control with high transmission, thus attracting growing scientific and technological attention for electomagnetic wave manipulation [1–4]. Owing to their low intrinsic losses compared to their metallic/plasmonic counterparts, as well as to the large refractive index difference with their surroundings, dielectric nanoscatterers are able to support strong resonant modes with the optical energy being strongly concentrated inside each nanoscatterer [5,6]. An essential building block for the realization of high-contrast all-dielectric metasurfaces is a silicon nanoscatterer [7]. This type of metasurface, i.e., silicon-based one, utilizes the dielectric properties of silicon characterized by negligible absorption and a high refractive index of $n = 3.5$ throughout the entire telecom spectral range. Various optical functionalities have been demonstrated utilizing all-dielectric silicon metasurfaces such as meta-lenses [8–12], holograms [6,13,4], vortex beam generators [15], beam deflectors [5,16,17] and also controlling of phase and polarization independently [6,14].

Recently, all-silicon dielectric metasurfaces have also been demonstrated to operate as basic optical elements such as polarization filters [18–22], vortex beam generators [23,24], holograms [25], Fresnel lenses [26], micro-lenses [27,28], metasurfaces supporting toroidal modes [29], as well as Pancharatnam–Berry phase elements for asymmetric transmission [30] offering excellent compatibility with complementary metal-oxide semiconductor processes and thus providing an efficient way for the development of compact optical devices for mid- and long-wavelength infrared technology. In most cases, for the realization of all-silicon dielectric metasurfaces, a conventional silicon microfabrication method is utilized that includes the combination of mask photolithography with reactive ion etching. However, this method requires expensive masks and multiple preprocesses, such as planarization and bonding, in order to obtain photoresist patterns with better quality.

In this work, ultrafast laser processing of silicon below ablation threshold in combination with subsequent wet chemical etching is utilized in order to realize all-silicon dielectric metasurfaces that can be produced in a single lithographical step. The method exploits the formation of the difference of etching rate between laser-modified and untreated regions for 2D micro/nanostructures to be generated [31–34]. Here, we take advantage of the quadrilateral orientation of the [100]-silicon crystal to fabricate silicon truncated cones (TC) and hollow truncated cones (HTC) and show the possibility to utilize them as the basic building blocks for the generation of all-silicon dielectric metasurfaces. This is the first time, to our knowledge, to show

the possibility to effectively realize all-silicon dielectric metasurfaces in a facile and cost-efficient manufacturing approach, with high throughput.

Materials and Methods

Experimental design

All-silicon dielectric metasurfaces are realized employing single-pulse femtosecond (fs) laser processing of silicon below ablation threshold in combination with subsequent wet chemical etching [31–34]. More specifically, the fabrication approach is a 2-step process and is illustrated schematically in Fig. 1. In the first step, the sample, which is a bare Si wafer, is irradiated by a focused single-pulse fs laser beam with pulse fluence below the ablation threshold. Prior to laser processing, the sample is treated with ethanol and further rinsed with 2-propanol in order to eliminate the organic pollutants. In a second step, the treated wafers are etched in a KOH solution (etchant) to form 2D controllable micro/nanostructures. An Yb:KGW Pharos-XP (Light Conversion) solid-state laser is utilized as a laser source, emitting at $\lambda = 1026$ nm central wavelength, with a repetition rate of 1 kHz and a pulse width of 170 fs. The laser fluence in our experiments can be adjusted by utilizing a combination of a half-wave plate and a polarizer. The substrates employed are standard single-side-polished, p-type, undoped <100>-oriented silicon wafers with 250-μm thickness. A 40× microscope objective lens (Zeiss, Plan Apochromat, numerical aperture = 0.95) is used to focus the laser beam onto the sample surface. The silicon specimen is mounted on an XYZ platform, which is computer-controlled. The XY axes (Aerotech, ANTXY130-110) have an encoder resolution of 1 nm and an accuracy of ±225 nm, while the Z stage (PI, M-112) moves asynchronously to the XY and has an accuracy of ±2 μm. The number of pulses delivered to the sample at specific distances is achieved by taking advantage of the internal pulse picker of Pharos XP laser with pulse on demand operation in combination with the use of Part Speed PSO (Position Synchronized Output) of the Aerotech Stages in order to synchronize the motion of the stages with the firing of the laser. The average fluence of the incidence laser pulse is in the range of 0.5 to 1 J/cm^2. The alkaline etchant composition of KOH (20%) and isopropyl alcohol (4%) in a volume ratio of 4:1 at 55 °C in air is utilized to etch wafers for 3 to 15 min [32,33]. In order to characterize the surface morphology of the laser processed silicon surface and the subsequent etched surface structures, an optical microscope and a scanning electron microscope (SEM) are employed.

In Fig. 1 (left, below), an optical microscopy image of a uniform array of nanodots fabricated by fs laser processing of silicon below ablation threshold is illustrated. As one can see, after irradiation with a single-pulse fs laser, the laser-modified region is demonstrated as bright dot-shaped areas featuring increased reflectivity in relation to the nonirradiated one as fs laser processing of silicon below ablation threshold causes crystalline silicon phase transition to an amorphous state. Depending on the intensity distribution of a Gaussian laser beam, the surface morphology of this induced thin layer of amorphous silicon can vary [32,33]; at large pulse fluence (~1 J/cm^2), a hollow-shaped modified area is formed (see Fig. S1A). As the laser pulse fluence decreases (~0.5 J/cm^2), the modified area decreases correspondingly. The central hollow-shaped area gradually becomes smaller, thus enabling the creation of features smaller than the focused spot (Fig. S1B) until it is totally suppressed. Considering that KOH has a quite different etching rate toward amorphous and crystalline silicon, this induced thin layer of amorphous silicon is used as an etch stop in a following wet chemical etching step. Therefore, depending on laser fluence and etching time, several 2D micro/nanostructures can be fabricated in a controllable manner [32]. Interestingly, because of the anisotropic etching of a patterned (100) Si surface in alkali solutions, the generated 2D micro/nanostructures present internal quadrilateral shapes [32,35]. Consequently, in our case, the initially formed uniform nanodots result in the generation of silicon TC after wet chemical etching in KOH solution, as illustrated in an optical microscopy image in Fig. 1 (right, below).

Theoretical calculations

A commercial 3-dimensional full-wave electromagnetic simulations solver (CST Microwave Studio) is used for modeling of the silicon TC, where the refractive index for bulk silicon (Si) was employed according to Palik [36]. Figure 2A illustrates SEM images (top and side view) of a single silicon TC fabricated by ultrafast laser processing of silicon below ablation threshold in combination with subsequent wet chemical etching. Figure 2B illustrates a schematic of a silicon TC structure arranged in a tetragonal lattice that was used as the basic meta-atom for numerical calculations. For single-cell (meta-atom) design, the unit cell boundary condition was employed along the x- and y-directions, while open boundary is set in the z-direction. An x-polarized normally incident plane wave was used to excite the structure from the substrate side. The substrate material is considered to be vacumn. The parameters employed for simulating the silicon TC were the following: The 2 bases of the silicon TC have a total width equal to D and d for the bottom and top surfaces, respectively. The walls are slanted at an angle $\theta = 35.3°$ due to the anisotropic etching of a patterned (100) Si surface in alkali solutions [32,35]. By simple trigonometry, the dimensions of the silicon TC are connected via the relation

$$p = 2htan(\theta) + d \quad (1)$$

where p is the period of the tetragonal lattice and h is the height of the silicon TC.

Optical measurements

Fourier transform infrared spectroscopy (FTIR) transmission/reflection spectra of the fabricated all-silicon dielectric metasurfaces were measured with a Vertex 80 spectrometer coupled to a Hyperion 2000 IR microscope (Bruker Optics), which was equipped with Cassegrain objectives (15× and 36×) and a liquid-nitrogen-cooled mercury cadmium telluride detector. Transmission/reflection measurements for linearly polarized light are carried out by inserting 2 custom-ordered waveplates with a retardation of λ/2 at wavelengths from 2 to 15 μm (Bruker Optics) into the beam path before and after the sample. All transmission/reflection spectra are normalized with respect to an unstructured region of the silicon wafer next to the fabricated silicon meta-atoms, as applied elsewhere [19].

Results and Discussion

Fabrication of all-silicon dielectric metasurfaces and optical characterization

Figure 3 shows SEM images of silicon TC generated by ultrafast laser processing of silicon below ablation threshold in

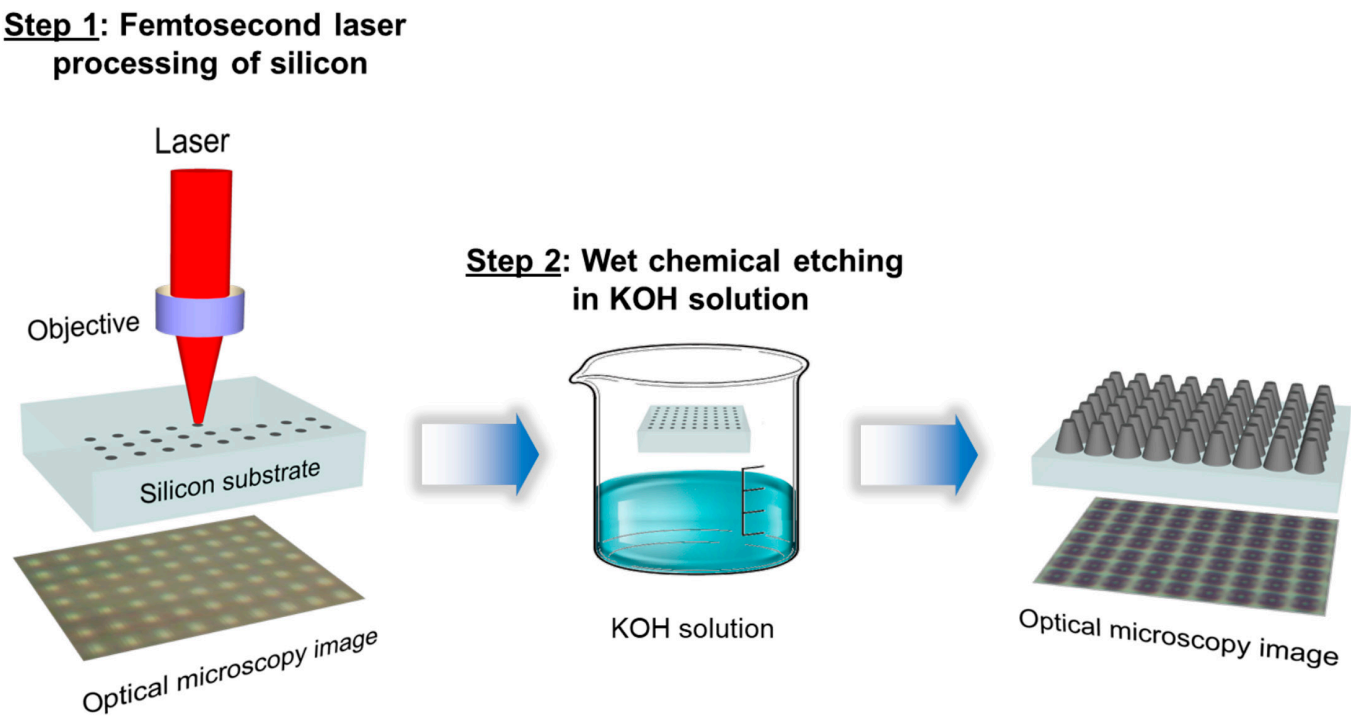

Fig. 1. Fabrication approach for all-silicon dielectric metasurfaces. 2D micro/nanostructures are generated by ultrafast laser processing of silicon below ablation threshold in combination with subsequent wet chemical etching. An optical microscopy image of a uniform array of nanodots fabricated by laser processing of silicon below ablation threshold (left, below) and the resulted generated silicon TC after wet chemical etching in KOH solution (right, below).

combination with subsequent wet chemical etching. The oblique and top views of an array of silicon TC with a footprint of 200 μm × 200 μm and with a periodicity of $p = 2.42$ μm along the x- and y-directions demonstrate the excellent structural quality of the fabricated structures. The diameter of the top surface of the fabricated silicon TC is approximately $d = 380$ nm, while the height is $h \sim 0.95$ μm. Also, a cross-sectional profile SEM image is provided in Fig. S. The generated silicon TC are regular in size and shape throughout the whole processed area indicating the high efficiency of the fabrication process.

Transmission (solid) and reflection (dashed) measurements for a linearly polarized light passing through a 200 μm × 200 μm uniform array of silicon TC are plotted in Fig. 4. The measurements were carried out at normal incidence in the spectral region from 2.4 to 15 μm with the light traveling in the z-direction incident from the bottom (substrate side). As one can see, when a linearly polarized light impinges on the fabricated array of silicon TC with diameter of the top surface $d = 220$ nm (dark yellow), 380 nm (blue), and 740 nm (red), 2 resonances appear that are clearly visible as a pronounced dip in transmission and a peak in reflection; the first resonance red-shifts from 4 to 4.5 μm and then to 5 μm, respectively, while the second one is slightly red-shifted from 2.8 to 3 μm and then to 3.2 μm, respectively. The height of the TC is approximately $h \sim 0.95$ μm (as shown in Fig. 3D), while the period of the array is set to $p = 2.42$ μm in both x- and y-directions. SEM images of the respective fabricated arrays of silicon TC are depicted on the right. Owing to the symmetry of the cylindrical TC, the transmission responses are polarization-independent (see Fig. S2).

Next, theoretical calculations that were performed using CST Microwave Studio employing a silicon TC as the basic meta-atom (as depicted in Fig. 2) are shown in Fig. 5. In particular, Fig. 5A illustrates simulated transmission of a uniform array of silicon TC as a function of the cone top diameter d and the wavelength. A color scale representing the range of transmission values is displayed on the right panel. The TC height is set to $h = 1$ μm and the period of the array is set to $p = 2.42$ μm in both x- and y-directions. The colored solid lines indicate the spectra of the silicon TC with cone top diameter d as selected in Fig. 4. In particular, in Fig. 5B, simulated transmission for the case of a silicon TC with cone top diameter $d = 740$ nm is shown (the corresponding experimental spectra are displayed as a red-colored line in Fig. 4). As one can see, the experimental data successfully reproduce the 2 transmission minima calculated in the theoretical simulations, showing only a slight offset regarding the position of the resonances. More specifically, theoretical calculations performed for the case of a silicon TC with cone top diameter $d = 740$ nm (Fig. 5B) predict the appearance of 2 resonances—one located at 4.3 μm and the other one at 3 μm—which are only slightly blue-shifted in relation to the experimental data, where the resonances are located at 5 and 3.2 μm, respectively (see Fig. 4, red-colored line). In the inset of Fig. 5B, the simulated side views (Z-X planes) of the magnetic energy density distributions in the silicon TC at 4.3 μm (brown solid line) and at 3 μm (gray solid line) under normal incidence is illustrated. In addition, as the diameter of the top surface d of the TC increases, the resonances are spectrally red-shifted (Fig. 5A); by gradually varying the cone top diameter d from 200 to 1000 nm, the first resonance moves from ~3.7 to ~4.8 μm, while the second one moves from ~2.5 to ~3.3 μm, which is in agreement with the experimental data shown in Fig. 4. Sample imperfections such as irregularities in the size of meta-atoms have a direct influence on the optical properties of the metasurfaces, resulting in a

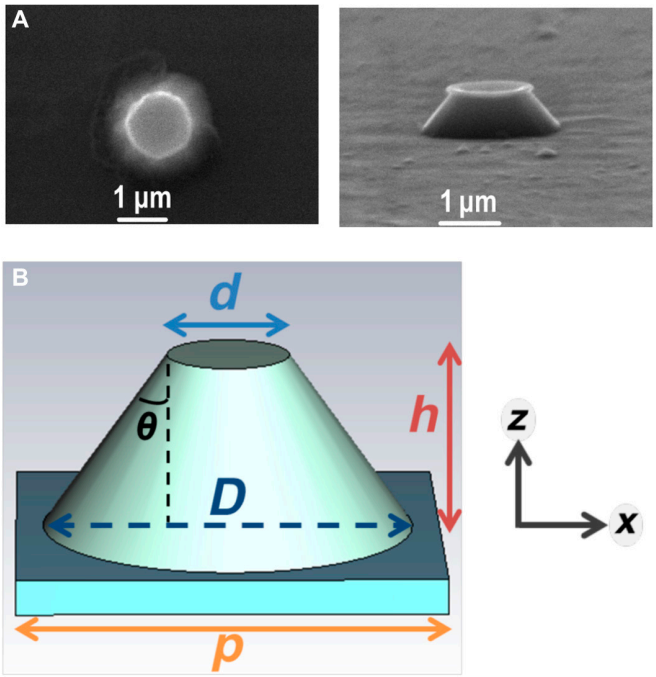

Fig. 2. Basic meta-atom: silicon TC. (A) SEM images (top and side view) of a silicon TC fabricated by ultrafast laser processing of silicon below ablation threshold in combination with subsequent wet chemical etching. (B) Schematic of a silicon TC unit cell that was used for numerical calculations. The walls are slanted at an angle $\theta = 35.3°$ because of the anisotropic etching of a patterned (100) Si surface in alkali solutions.

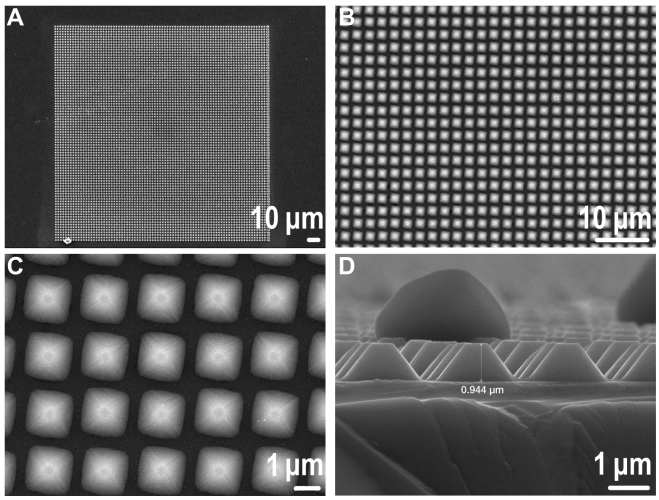

Fig. 3. SEM images of silicon TC generated by ultrafast laser processing of silicon below ablation threshold in combination with subsequent wet chemical etching. (A) Overview of a 200 μm × 200 μm uniform array of silicon TC with cone top diameter $d = 380$ nm. The height of the TC is approximately $h \sim 0.95$ μm, while the period of the array is set to $p = 2.42$ μm in both x- and y-directions. (B and C) Overview at higher magnification and (D) side view.

broader and less pronounced as well as an overall lower transmittance in relation to the theoretically calculated values.

Furthermore, the response of the meta-atoms is scalable; by varying the unit-cell size of the silicon TC either by changing the height h, the cone top diameter d, or the period p, the metasurface's resonant frequencies can be shifted in a controllable manner.

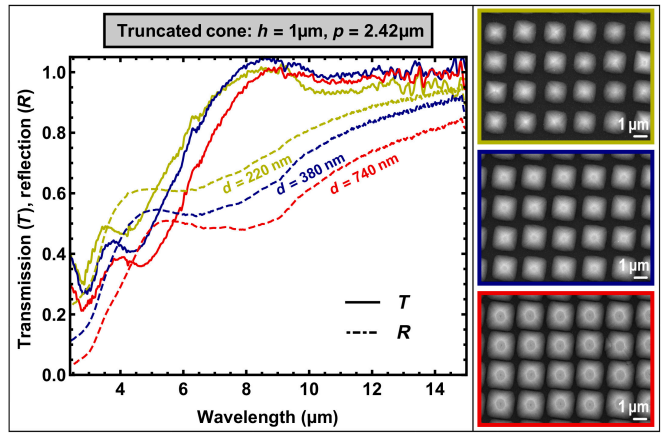

Fig. 4. FTIR measurements of the fabricated silicon TC for linearly polarized incident light. Measured transmission (solid) and reflection (dashed) response of a 200 μm × 200 μm uniform array of silicon TC with cone top diameter $d = 220$ nm (dark yellow), $d = 380$ nm (blue) and $d = 740$ nm (red). The height of the TC is approximately $h \sim 0.95$ μm (shown in Fig. 3), while the period of the array is set to $p = 2.42$ μm in both x- and y-directions. Right: SEM images of the respective fabricated arrays of silicon TC.

Figure S3 shows transmission (solid) and reflection (dashed) measurements for linearly polarized incident light for the case of 3 different uniform arrays of silicon TC, where the unit cell size increases by varying the height h of the silicon meta-atom. SEM images of the respective fabricated arrays of silicon TC are displayed on the right, while theoretical calculations are displayed in Fig. S4 showing a similar trend regarding the position of the resonances in comparison with the experimental data (shown in Fig. S3).

Moreover, silicon HTC (illustrated in Fig. S5B) can also be generated in a similar manner, simply by exploiting the hollow-shaped modified area of the induced thin layer of amorphous silicon formed after single-pulse fs laser irradiation at large pulse fluence (see Fig. S1A). Next, using these silicon cones (truncated and hollow truncated) as basic building blocks, we propose an all-silicon dielectric metasurface device.

Antiferromagnetic order in an all-silicon dielectric metasurface

Inspired by the theoretical investigations on near-field coupling effects for dissimilar Mie-resonant dielectric meta-atoms in all-dielectric metasurfaces discussed by Lepeshov and Kivshar in [37], we construct an asymmetric dimer consisting of a silicon TC and a hollow truncated one and investigate the possibility for optically induced magnetic moments that can possess antiferromagnetic (AFM) order. The underlying mechanism for induced optical magnetism in dielectric particles is the excitation of resonant modes that support circulating displacement currents leading, in turn, to magnetic dipole moments. When the coupling between neighboring meta-atoms cannot be neglected, excitation of a certain meta-atom may subsequently induce magnetic dipole moments in nearby meta-atoms [37–40]. By changing the coupling strength (e.g., by changing the distance between the individual meta-atoms [41]) in-phase or out-of-phase moments can be excited, leading to AFM- or ferromagnetic-type response, respectively. In our case, the geometrical parameters of the silicon TC and the HTC are chosen so as to create resonant configuration when the magnetic resonance of a TC overlaps with a slope of the magnetic resonance of an HTC as discussed

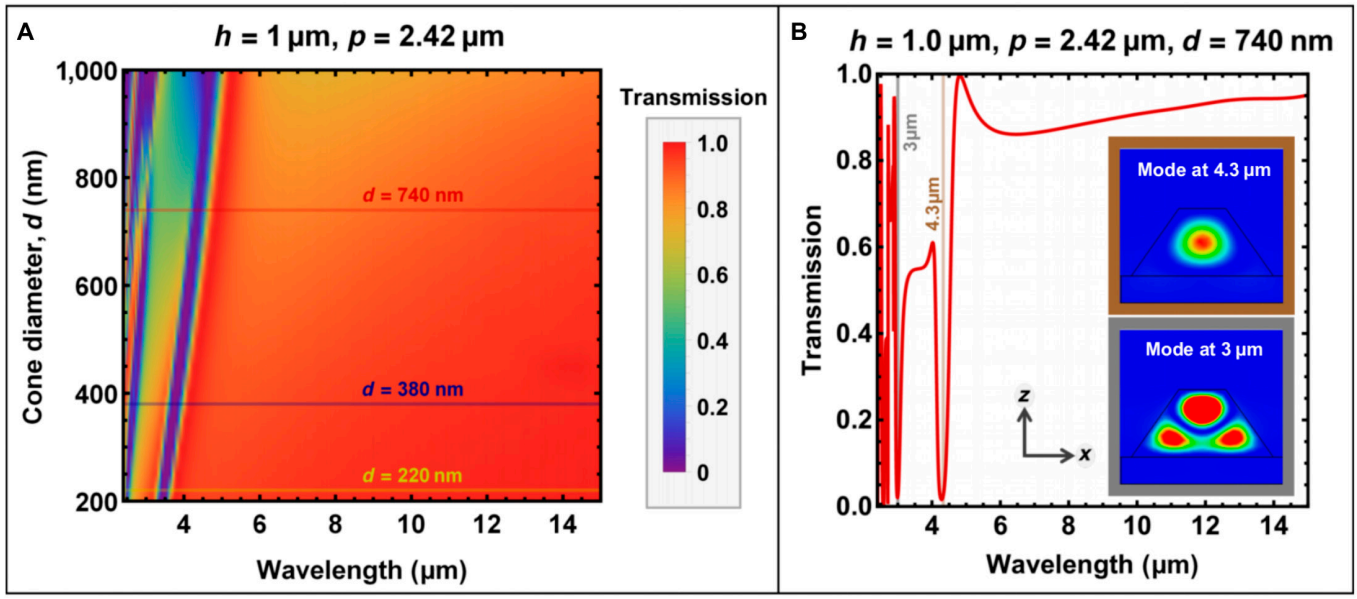

Fig. 5. Theoretical calculations for a silicon TC meta-atom. (A) Simulated transmission of a uniform array of silicon TC as a function of the cone top diameter, d, and the wavelength. A color scale representing the range of transmission values is shown on the right panel. The TC height is set to $h = 1$ μm and the period of the array is set to $p = 2.42$ μm in both x- and y-directions. The colored solid lines indicate the spectra of the silicon TC with cone top diameter d as selected in Fig. 4; the one selected in [B]) is for the case of $d = 740$ nm. (B) Simulated transmission of a silicon TC with cone top diameter $d = 740$ nm. (Inset) Magnetic energy density distributions in the silicon TC at the wavelength of 4.3 μm (brown solid line) and 3 μm (gray solid line). An x-polarized plane wave is normally incident on the silicon TC from the bottom (substrate side).

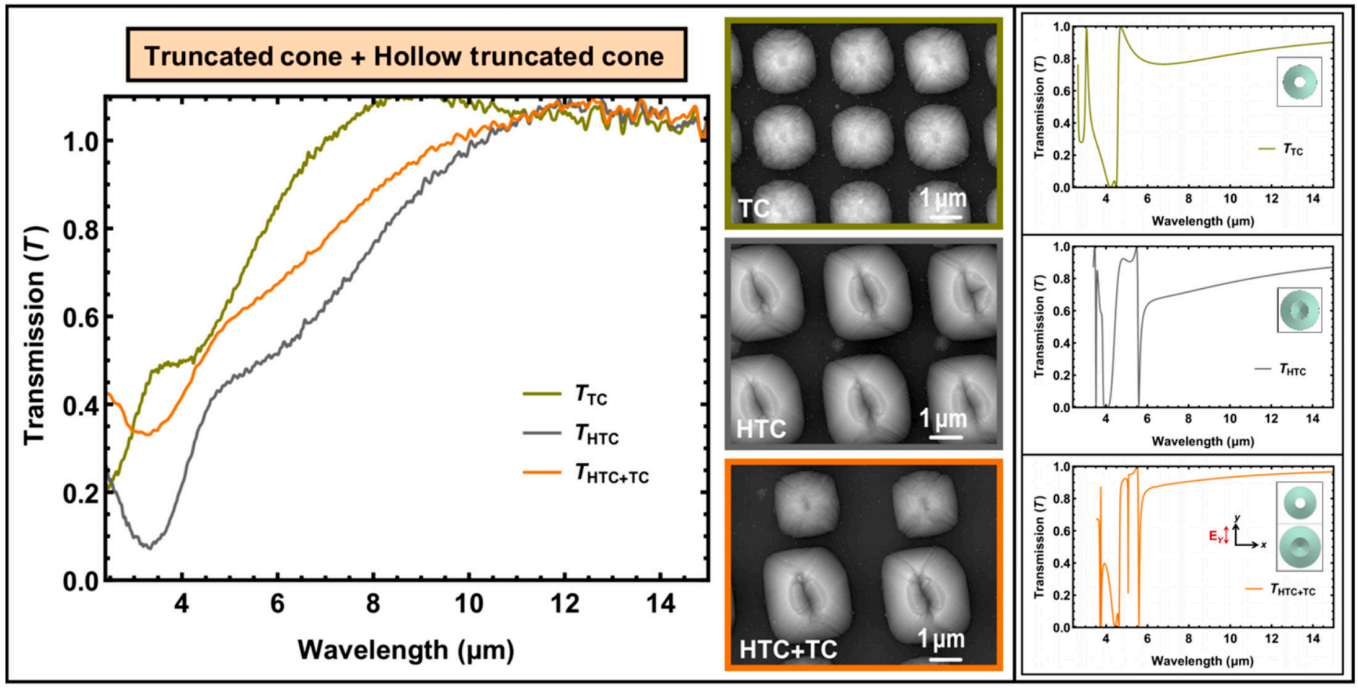

Fig. 6. FTIR measurements and theoretical simulations for an asymmetric dimmer consisting of a silicon truncated cone (TC) and a hollow truncated cone (HTC). (Left panel) Measured transmission for an y- normally incident linearly polarized light onto an array of silicon TC (green), an array of HTC (gray) and an array of an asymmetric dimmer consisting of a silicon TC and an HTC (HTC+TC, orange) with identical geometrical characteristics as the individual meta-atoms. SEM images of the respective arrays are illustrated in the inset. The height of the fabricated structures is approximately $h \sim 0.97$ μm (see Fig. S5), while the period of the arrays is set to $p_{TC} = 2.42$ μm and $p_{HTC} = 3.42$ μm, respectively, in both x- and y-directions. (Right panel) Simulated transmission for the case of a silicon TC meta-atom with cone top diameter $d_{TC} = 400$ nm (green), an HTC with cone top diameter $d_{HTC} = 1.6$ μm (gray) and an asymmetric dimmer (orange) are illustrated. A y-polarized plane wave is normally incident on the silicon cones from the bottom (substrate side).

by Lepeshov and Kivshar in [37] and similarly reported in a previous work [40].

Figure 6 (inset) illustrates SEM images of the fabricated arrays of silicon cones; an array of TC, an array of HTC and an array of an asymmetric dimmer consisting of a TC and an HTC (HTC+TC) with identical geometrical characteristics as the individual meta-atoms. The fabricated arrays have a footprint of 200 μm × 200 μm (see also Fig. S5). Transmission measurements for a *y*-linearly polarized light normally incident onto the fabricated structures are illustrated on the left panel of Fig. 6, while the respective theoretical calculations are shown on the right panel. In the theoretical calculations, the TC top diameter is set to $d = 400$ nm and the array periodicity is set to $p = 2.42$ μm in both *x*- and *y*-directions. A schematic of the unit cell of the HTC is shown in Fig. S6A. The outer top diameter of the HTC is $d_{\mathrm{HTC}} = 1.6$ μm, the inner is set to $d_{in} = 1.4$ μm, and the array periodicity is set to $p_{\mathrm{HTC}} = 3.42$ μm along the *x*- and *y*-directions. The simulated side view (Z-X plane) of the magnetic energy density distribution in the silicon HTC at 4 μm under normal incidence is illustrated in Fig. S6B. The height of both cones is set to $h = 1$ μm, which is close to the experimental value obtained, i.e., $h \sim 0.97$ μm (see Fig. S5D). Individual transmittance measurements of the fabricated metasurfaces show features at ~4.5 μm and at ~3.5 μm for the fabricated TC (green line) and the HTC (gray line), respectively. Theoretical calculations predict a magnetic mode at 4.3 μm and at 4 μm for the TC (green line) and HTC (gray line), respectively, both of which are manifested as transmittance dips at the respective wavelengths in accordance with our experimental observations. When both meta-atoms are combined into an asymmetric dimmer, the magnetic response in the theoretically calculated data demonstrates a splitting of resonances at 4 μm responsible for the formation of the AFM order [40], while in the experimental data (orange line) a conjugated mode is observed.

Conclusion

In conclusion, we report on the realization of all-silicon dielectric metasurfaces, utilizing a facile and cost-efficient method, which is based on single-pulse fs laser processing of silicon below ablation threshold in combination with subsequent wet chemical etching. The fabrication approach relies on the formation of a thin layer of amorphous silicon induced by fs laser irradiation below ablation threshold, which acts as an etch-stop masking in the KOH etching process. By tuning the laser pulse fluence, different morphologies can be laser-printed, enabling the fabrication of various functional 2D silicon micro/nanostructures. Here, we have demonstrated the fabrication of truncated and HTC, as well as hybrid metasurfaces with AFM response consisting of both types of nanocones, all generated in one lithographical step. Single-pulse fs laser irradiation of silicon below ablation threshold is particularly suitable for the rapid fabrication of large-area patterned silicon surfaces and is, therefore, very promising for integration on a photonic chip and mass production.

Acknowledgments

The authors would like to thank Dr. G. Kenanakis for providing access to FTIR spectrometer. **Funding:** This work was supported by the EU's H2020 framework program for research and innovation under the NFFA-Europe-Pilot project (Grant No. 101007417). **Author contributions:** All authors contributed equally to the writing of the manuscript. **Competing interests:** The authors declare that there are no competing interests.

Data Availability

Data is available on request.

Supplementary Materials

Supplementary figures are available in Supplementary Materials.

References

1. Kamali SM, Arbabi E, Arbabi A, Faraon A. A review of dielectric optical metasurfaces for wavefront control. *Nanophotonics*. 2018;7(6):1041–1068.
2. Duan H, Wang X, Luo X, Ou X, Li L, Chen Y, Yang P, Wang S, Duan H. All-dielectric metasurfaces for polarization manipulation: Principles and emerging applications. *Nanophotonics*. 2020;9(12):3755–3780.
3. Tanyi Ako R, Upadhyay A, Withayachumnankul W, Bhaskaran M, Sriram S. Dielectrics for terahertz metasurfaces: Material selection and fabrication techniques. *Adv Opt Mater*. 2020;8(3):Article 1900750.
4. Brener I, Liu S, Staude I, Valentine J, Holloway CL. *Dielectric metamaterials: Fundamentals, designs, and applications*. Cambridge (UK): Woodhead Publishing; 2019.
5. Khorasaninejad M, Capasso F. Broadband multifunctional efficient meta-gratings based on dielectric waveguide phase shifters. *Nano Lett*. 2015;15(10):6709–6715.
6. Arbabi A, Horie Y, Bagheri M, Faraon A. Dielectric metasurfaces for complete control of phase and polarization with subwavelength spatial resolution and high transmission. *Nat Nanotechnol*. 2015;10(11):937–943.
7. Staude I, Schilling J. Metamaterial-inspired silicon nanophotonics. *Nat Photonics*. 2017;11(5):274–284.
8. Kamali SM, Arbabi E, Arbabi A, Horie Y, Faraon A. Highly tunable elastic dielectric metasurface lenses. *Laser Photonics Rev*. 2016;10(6):1002–1008.
9. Arbabi A, Horie Y, Ball AJ, Bagheri M, Faraon A. Subwavelength-thick lenses with high numerical apertures and large efficiency based on high-contrast transmitarrays. *Nat Commun*. 2015;6(1):Article 7069.
10. Chantakit T, Schlickriede C, Sain B, Meyer F, Weiss T, Chattham N, Zentgraf T. All-dielectric silicon metalens for two-dimensional particle manipulation in optical tweezers. *Photonics Res*. 2020;8(9):1435–1440.
11. Kamali SM, Arbabi A, Arbabi E, Horie Y, Faraon A. Decoupling optical function and geometrical form using conformal flexible dielectric metasurfaces. *Nat Commun*. 2016;7(1):Article 11618.
12. Khorasaninejad M, Zhu AY, Roques-Carmes C, Chen WT, Oh J, Mishra I, Devlin RC, Capasso F. Polarization-insensitive metalenses at visible wavelengths. *Nano Lett*. 2016;16(11):7229–7234.
13. Khorasaninejad M, Ambrosio A, Kanhaiya P, Capasso F. Broadband and chiral binary dielectric meta-holograms. *Sci Adv*. 2016;2(5):Article e1501258.
14. Overvig AC, Shrestha S, Malek SC, Lu M, Stein A, Zheng C, Yu N. Dielectric metasurfaces for complete and independent control of the optical amplitude and phase. *Light Sci Appl*. 2019;8(1):Article 92.

15. Chong KE, Staude I, James A, Dominguez J, Liu S, Campione S, Subramania GS, Luk TS, Decker M, Neshev DN, et al. Polarization-independent silicon metadevices for efficient optical wavefront control. *Nano Lett*. 2015;15(8):5369–5374.
16. Aoni RA, Rahmani M, Xu L, Kamali KZ, Komar A, Yan J, Neshev D, Miroshnichenko AE. High-efficiency visible light manipulation using dielectric metasurfaces. *Sci Rep*. 2019;9(1):Article 6510.
17. Sell D, Yang J, Doshay S, Yang R, Fan JA. Large-angle, multifunctional metagratings based on freeform multimode geometries. *Nano Lett*. 2017;17(6):3752–3757.
18. Zi J, Xu Q, Wang Q, Tian C, Li Y, Zhang X, Han J, Zhang W. Antireflection-assisted all-dielectric terahertz metamaterial polarization converter. *Appl Phys Lett*. 2018;113(10):Article 101104.
19. Dong Y, Xu Z, Li N, Tong J, Fu YH, Zhou Y, Hu T, Zhong Q, Bliznetsov V, Zhu S, et al. Si metasurface half-wave plates demonstrated on a 12-inch CMOS platform. *Nanophotonics*. 2019;9(1):149–157.
20. Zhang H, Zhang X, Xu Q, Tian C, Wang Q, Xu Y, Li Y, Gu J, Tian Z, Ouyang C, et al. High-efficiency dielectric metasurfaces for polarization-dependent terahertz wavefront manipulation. *Adv Opt Mater*. 2018;6(1):Article 1700773.
21. Xu Z, Dong Y, Tseng C-K, Hu T, Tong J, Zhong Q, Li N, Sim L, Lai KH, Lin Y, et al. CMOS-compatible all-Si metasurface polarizing bandpass filters on 12-inch wafers. *Opt Express*. 2019;27(18):26060–26069.
22. He Y, Wang L, Wu T, Wu Z, Chen Y, Yin K. Facile fabrication of hierarchical textures for substrate-independent and durable superhydrophobic surfaces. *Nanoscale*. 2022;14:9392–9400.
23. Zhang H, Zhang X, Xu Q, Wang Q, Xu Y, Wei M, Li Y, Gu J, Tian Z, Ouyang C, et al. Polarization-independent all-silicon dielectric metasurfaces in the terahertz regime. *Photonics Res*. 2018;6(1):24–29.
24. Dharmavarapu R, Izumi K, Katayama I, Ng SH, Vongsvivut J, Tobin MJ, Kuchmizhak A, Nishijima Y, Bhattacharya S, Juodkazis S. Dielectric cross-shaped-resonator-based metasurface for vortex beam generation at mid-IR and THz wavelengths. *Nanophotonics*. 2019;8(7):1263–1270.
25. Wu T, Zhang X, Xu Q, Plum E, Chen K, Xu Y, Lu Y, Zhang H, Zhang Z, Chen X, et al. Dielectric metasurfaces for complete control of phase, amplitude, and polarization. *Adv Opt Mater*. 2022;10(1):Article 2101223.
26. Minkevičius L, Indrišiūnas S, Šniaukas R, Voisiat B, Janonis V, Tamošiūnas V, Kašalynas I, Račiukaitis G, Valušis G. Terahertz multilevel phase Fresnel lenses fabricated by laser patterning of silicon. *Opt Lett*. 2017;42(10):1875–1878.
27. Liu M, Fan Q, Yu LE, Xu AT. Polarization-independent infrared micro-lens array based on all-silicon metasurfaces. *Opt Express*. 2019;27(8):10738–10744.
28. Zhu Y, Zhoua S, Wang Z, Pu X, Cao X, Yu Y, Yuan W, Liu W. High-efficiency all-silicon metasurfaces with 2π phase control based on multiple resonators. *Results Phys*. 2021;29:Article 104765.
29. Zografopoulos DC, Ferraro A, Algorri JF, Martín-Mateos P, García-Cámara B, Moreno-Oyervides A, Krozer V, Acedo P, Vergaz R, Sánchez-Pena JM, et al. All-dielectric silicon metasurface with strong subterahertz toroidal dipole resonance. *Adv Opt Mater*. 2019;7(19):Article 1900777.
30. Kenney M, Li S, Zhang X, Su X, Kim TT, Wang D, Wu D, Ouyang C, Han J, Zhang W, et al. Pancharatnam-berry phase induced spin-selective transmission in herringbone dielectric metamaterials. *Adv Mater*. 2016;28(43):9567–9572.
31. Huang J, Jiang L, Li X, Wang A, Wang Z, Wang Q, Hu J, Qu L, Cui T, Lu Y. Fabrication of highly homogeneous and controllable nanogratings on silicon via chemical etching-assisted femtosecond laser modification. *Nanophotonics*. 2019;8(5):869–878.
32. Li X, Xie Q, Jiang L, Han W, Wang Q, Wang A, Hu J, Lu Y. Controllable Si (100) micro/nanostructures by chemical-etching-assisted femtosecond laser single-pulse irradiation. *Appl Phys Lett*. 2017;110(18):Article 181907.
33. Kiani A, Venkatakrishnan K, Tan B. Micro/nano scale amorphization of silicon by femtosecond laser irradiation. *Opt Express*. 2009;17(19):16518–16526.
34. Chen F, Yang Q, Chen F, Meng X, Bian H, Yong J, Shan C, Hou X. Fabrication of large-area concave microlens array on silicon by femtosecond laser micromachining. *Opt Lett*. 2015;40(9):1928–1931.
35. Fan Y, Han P, Liang P, Xing Y, Ye Z, Hu S. Differences in etching characteristics of TMAH and KOH on preparing inverted pyramids for silicon solar cells. *Appl Surf Sci*. 2013;264:761–766.
36. Palik ED. *Handbook of optical constants of solids*. Cambridge (MA): Elsevier Inc.; 2012.
37. Lepeshov S, Kivshar Y. Near-field coupling effects in Mie-resonant photonic structures and all-dielectric metasurfaces. *ACS Photonics*. 2018;5(7):2888–2894.
38. Kivshar Y, Roberts AP. Classical and exotic magnetism: Recent advances and perspectives. *Low Temp Phys*. 2017;43(8):895–900.
39. Tuz VR, Yu P, Dmitriev V, Kivshar YS. Magnetic dipole ordering in resonant dielectric metasurfaces. *Phys Rev Appl*. 2020;13(4):Article 044003.
40. Miroshnichenko AE, Filonov D, Lukyanchuk B, Kivshar Y. Antiferromagnetic order in hybrid electromagnetic metamaterials. *New J Phys*. 2017;19(8):Article 083013.
41. Miroshnichenko AE, Lukyanchuk B, Maier SA, Kivshar YS. Optically induced interaction of magnetic moments in hybrid metamaterials. *ACS Nano*. 2012;6(1):837–842.